Observations and Predictability of a High-Impact Narrow Cold-Frontal Rainband over Southern California on 2 February 2019

FOREST CANNON

Center for Western Weather and Water Extremes, and Scripps Institution of Oceanography, University of California, San Diego, La Jolla, California

NINA S. OAKLEY

Western Regional Climate Center, Desert Research Institute, Reno, Nevada

CHAD W. HECHT AND ALLISON MICHAELIS

Center for Western Weather and Water Extremes, and Scripps Institution of Oceanography, University of California, San Diego, La Jolla, California

JASON M. CORDEIRA

Meteorology Program, Plymouth State University, Plymouth, New Hampshire

BRIAN KAWZENUK, REUBEN DEMIRDJIAN, RACHEL WEIHS, MEREDITH A. FISH, ANNA M. WILSON, AND F. MARTIN RALPH

Center for Western Weather and Water Extremes, and Scripps Institution of Oceanography, University of California, San Diego, La Jolla, California

(Manuscript received 22 January 2020, in final form 27 July 2020)

ABSTRACT: Short-duration, high-intensity rainfall in Southern California, often associated with narrow cold-frontal rainbands (NCFR), threaten life and property. While the mechanisms that drive NCFRs are relatively well understood, their regional characteristics, specific contribution to precipitation hazards, and their predictability in the western United States have received little research attention relative to their impact. This manuscript presents observations of NCFR physical processes made during the Atmospheric River Reconnaissance field campaign on 2 February 2019 and investigates the predictability of the observed NCFR across spatiotemporal scales and forecast lead time. Dropsonde data collected along transects of an atmospheric river (AR) and its attendant cyclone during rapid cyclogenesis, and radiosonde observations during landfall 24 h later, are used to demonstrate that a configuration of the Weather Research and Forecasting (WRF) Model skillfully reproduces the physical processes responsible for the development and maintenance of the impactful NCFR. Ensemble simulations provide quantitative uncertainty information on the representation of these features in numerical weather prediction and instill confidence in the utility of WRF as a forecast guidance tool for short- to medium-range prediction of mesoscale precipitation processes in landfalling ARs. This research incorporates novel data and methodologies to improve forecast guidance for NCFRs impacting Southern California. While this study focuses on a single event, the outlined approach to observing and predicting high-impact weather across a range of spatial and temporal scales will support regional water management and hazard mitigation, in general.

KEYWORDS: Cold fronts; Extratropical cyclones; Precipitation; In situ atmospheric observations; Ensembles; Mesoscale models

1. Introduction

Short-duration, high-intensity rainfall associated with cool season synoptic storm systems often threatens life, property, and infrastructure in Southern California. The Southern California Bight (~32.5°–34.5°N, ~120.5°–117°W; hereafter "the Bight"), extending from Santa Barbara County in the west to San Diego County in the southeast, is home to approximately 18 million people (U.S. Census Bureau 2019). The region's expansive urban development situates large populations on alluvial fans below steep and complex terrain, which renders the area vulnerable to a variety of short-duration high-intensity precipitation impacts such as post-wildfire debris flows (USGS 2005; Cannon et al. 2008; Staley et al. 2013; Oakley et al. 2017, 2018a), shallow landslides (Wills et al. 2017; Oakley et al. 2018b) and flash flooding (National Research Council 2005). Despite advances in numerical weather prediction (NWP), forecasting the location, intensity and duration of high intensity rainfall remains problematic. Furthermore, the performance of NWP forecast guidance products has not been established relative to these challenges. As a result, the National Weather Service (NWS) and emergency managers must rely heavily upon radar and near-real-time rain gauge networks to assess flash flood and debris flow hazards, despite

Corresponding author: Forest Cannon, fcannon@ucsd.edu

DOI: 10.1175/WAF-D-20-0012.1

their initiation being nearly simultaneous with the observation of short-duration, high-intensity precipitation (e.g., Kean et al. 2011). Thus, evaluating the potential of global and mesoscale ensemble forecasts to provide advanced warning of hazardous precipitation such that precautions may be taken to mitigate impacts is crucial to augmenting forecasts for protecting people, resources, and infrastructure in Southern California.

Meaningful thresholds for intensity and duration of rainfall are often regionally specific and can be tied to the underlying meteorological processes, spatial scale, and/or hydrologic impacts. The American Meteorological Society defines "heavy rainfall" as exceeding 7.62 mm h^{-1} (0.3 in. h^{-1}) (AMS 2012). The U.S. Geological Survey specifies a precipitation intensity > 24 mm h^{-1} (0.94 in. h^{-1}) for a duration of 15 min as a general baseline for triggering postwildfire debris flows in the Transverse Ranges of Southern California (USGS 2019). Herein, "short duration" is defined as subhourly to hourly time scales. There are several atmospheric mechanisms that may generate short-duration, high-intensity rainfall regionally (Oakley et al. 2017), including narrow cold-frontal rainbands (NCFR). NCFRs have a notable record of impacts in this region (Sukup et al. 2015; Oakley et al. 2017; Cannon et al. 2018), including the catastrophic postwildfire debris flow that killed 23 people and destroyed over 100 homes in Montecito, California, in 2018 (Oakley et al. 2018a).

NCFRs are recognizable in radar imagery as elongated bands of enhanced reflectivity (>40–50 dBZ) that are ~3–5 km wide and both parallel to and in proximity of a cold front (Hobbs 1978; Browning 1986; Jorgensen et al. 2003). These features may extend several hundred kilometers in length but are typically on the order of several tens of kilometers long and broken up into characteristic "gaps and cores" (e.g., Hobbs 1978; Browning 1986; Locatelli et al. 1995; Wakimoto and Bosart 2000; Jorgensen et al. 2003). The "cores" are areas of enhanced reflectivity (e.g., >40 dBZ and often exceeding 50 dBZ), strong upward vertical velocities, and intense rainfall, while "gaps" feature lighter rainfall and weaker vertical velocities. NCFRs have been both observed and modeled along the U.S. West Coast since the 1970s in various studies and field campaigns (e.g., Hobbs 1978; Hobbs and Persson 1982; Blier 2003; Jorgensen et al. 2003; Neiman et al. 2004; Persson et al. 2005; Houze et al. 2017; Cannon et al. 2018; Oakley et al. 2018a). The last field campaign to analyze these features in depth for Southern California prior to this study took place in 2001 (e.g., Jorgensen et al. 2003).

While the literature on the dynamics of NCFRs is substantial, there is a need to reconcile this information with observations and model guidance from previous events in a framework that can inform West Coast operational forecasting from synoptic to local scales and across lead times. Here we use novel data from the airborne Atmospheric River Reconnaissance 2019 field campaign (AR Recon; Cordeira et al. 2017; Ralph et al. 2020; Fig. 1), which performed targeted sampling of an NCFR collocated with a strong landfalling AR on 2 February 2019 using offshore dropsondes and onshore radiosondes (Fig. 1). This event caused sediment-laden flows on the 2017 Thomas Fire burn area (in Santa Barbara County) and debris flows on the 2018 Woolsey Fire burn area (in Ventura County)

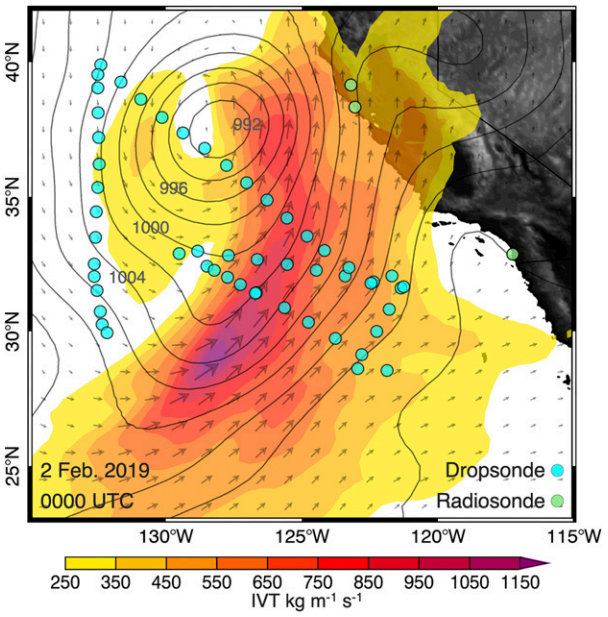

FIG. 1. Integrated vapor transport (filled contours; kg m^{-1} s^{-1}) and sea level pressure (gray contours; hPa) from Global Forecast System analysis at 0000 UTC 2 Feb 2019, 18 h preceding the appearance of an NCFR in radar observations in the Southern California Bight. AR Recon dropsonde locations from two U.S. Air Force C-130 aircraft flights within 3 h of the analysis time (cyan dots), radiosonde launch locations during the event (green dots), and topography (gray shade) are also shown.

that resulted in temporary closures of Highway 101 and Highway 1, respectively, in both directions. Numerous other road closures, vehicle crashes, and flash flooding associated with intense rainfall were reported across Southern California (CBS Los Angeles 2019; Parvini et al. 2019; Times Staff 2019). Sounding observations of the 2 February 2019 event enable an evaluation of the NCFR and support the subsequent diagnosis of dynamical processes that ultimately improve understanding of the NCFR's development and predictability.

In this paper, we 1) discuss the synoptic environment and its evolution with respect to an observed NCFR on 2 February 2019, and evaluate its predictability in global ensemble forecasts, 2) use observations from AR Recon (Fig. 1) to evaluate the representation and predictability of the observed NCFR in mesoscale ensemble simulations, 3) provide guidance for forecasting these events in an operational framework, and 4) highlight challenges operational forecasters may face in predicting impacts associated with these events. The goal of this work is to support forecasters' ability to provide decision support for emergency managers, flood control districts, and the public, related to short-duration, high-intensity precipitation associated with NCFRs. The analyses and discussion are relevant beyond Southern California, as the dynamical processes that drive NCFRs can be found globally in extratropical cyclones (e.g., Gatzen 2011; Norris et al. 2017). Insight into the predictability of these processes across spatial and temporal scales may be useful for forecasting NCFR occurrence in

midlatitude winter storms elsewhere, even if the specific impacts of short-duration high-intensity precipitation differ.

2. Data

a. Global Forecast System analysis

Synoptic meteorological conditions for the case study were investigated using the National Centers for Environmental Prediction (NCEP) Global Forecast System (GFS) Analysis. GFS data are available globally on a 0.5° latitude × 0.5° longitude horizontal grid every 6 h at 0000, 0600, 1200, and 1800 UTC throughout the study period. The GFS data were used to derive meteorological parameters commonly invoked in the analyses of landfalling ARs such as geopotential heights and wind at multiple isobaric levels, integrated water vapor (IWV), and integrated vapor transport (IVT; calculated for the column extending from the surface to 200 hPa). The data were also used to calculate vertical profiles of equivalent potential temperature, horizontal frontogenesis (Petterssen 1936) and 700–500-hPa **Q**-vector divergence (Hoskins et al. 1978; Hoskins and Peddler 1980) in order to assess dynamical forcing for ascent. The NCEP Global Ensemble Forecast System (GEFS) data were additionally used to determine forecast uncertainty for the large-scale meteorological features responsible for this case. The GEFS consists of 20 perturbed GFS ensemble members that are available with the same horizontal grid spacing and 6-hourly initialization schedule as GFS. Here, event sea level pressure (SLP) forecasts were evaluated out to 8-day lead time across all ensemble members.

b. AR Recon field campaign observations

The AR Recon field campaign is an annual airborne data collection effort led by the Center for Western Weather and Water Extremes at the Scripps Institution of Oceanography (SIO) in partnership with the U.S. Air Force (USAF) and multiple federal, state and academic entities. AR Recon has been active for four winter seasons, including 2016, 2018, 2019 and 2020 (Ralph et al. 2020). The first flights of the 2019 season occurred on 2 February 2019 and sampled the system discussed in this manuscript offshore of Southern California. A total of 60 dropsondes were released by two USAF C-130 aircraft with a goal of sampling profiles of temperature, humidity, pressure and winds proximal to the AR and dynamical features of the deepening cyclone. The mesoscale characteristics of the NCFR, which were suggested by mesoscale Weather Research and Forecasting (WRF) Model forecasts generated by SIO during flight planning, necessitated high-density observations with ~60-km spacing.

The offshore sampling by AR Recon aircraft was supplemented by profiles of temperature, humidity, pressure and winds from Vaisala RS-41 sondes launched from three coastal radiosonde launch locations. Sondes were released at 1.5-h intervals at two locations in Northern California and at SIO, near San Diego. During the NCFR passage over San Diego, several off-schedule sondes were launched at ~30-min intervals to sample the feature's low-level structure with high-temporal frequency. Only the sondes launched from San Diego immediately before and after the NCFR passage were evaluated here.

c. Conventional meteorological observations

Observations from radar and rain gauges were used to evaluate precipitation characteristics (e.g., intensity, areal coverage, and duration). Radar observations include 0.46° base reflectivity data from the San Diego (KNKX) NWS Next-Generation Weather Radar (NEXRAD; NOAA 1991) installation, available at ~5-min resolution. These radar data are essential to regional hazard forecasting at short lead times as they are frequently used by regional NWS forecasters to identify mesoscale features with intense precipitation rates before they propagate onshore (Gomberg et al. 2018). Unfortunately, the Santa Ana NEXRAD (KSOX) site was not operational at the time of the event. Additionally, precipitation observations at 5-min temporal resolution were acquired for several San Diego County Flood Control District ALERT gauges (County of San Diego 2019) that either did or did not experience the passage of a core of the NCFR to demonstrate the feature's impact on regional spatiotemporal precipitation distributions.

d. Mesoscale model

Version 3.9.1 of the WRF Model (Skamarock et al. 2008) was used to identify the mesoscale physical mechanisms responsible for the development of the NCFR. The model configuration used here employs an outer domain with 9-km horizontal grid spacing and an inner domain with 3-km grid spacing projected onto a Lambert conformal grid with 60 vertical levels and one-way feedback.

The parameterized physics options used in the control simulation included the Rapid Radiative Transfer Model (RRTM; Mlawer et al. 1997), which was used for both shortwave and longwave spectral bands, the revised MM5 surface layer scheme (Jimenez et al. 2012), the YSU planetary boundary layer scheme (Hong et al. 2006), the new Thompson microphysics scheme (Thompson et al. 2008), and the scale-aware Grell-3D convective parameterization scheme (Grell and Devenyi 2002), which was only used in the outer domain. The domain and selected physics were based on "West-WRF"—a WRF configuration that was specifically developed for the improved representation of AR characteristics and their associated precipitation (Martin et al. 2018). West-WRF is implemented in near–real time at the Center for Western Weather and Water Extremes at SIO for situational awareness (https://cw3e.ucsd.edu/). Here, WRF was initialized at 0000 UTC 1 February 2019 and forced with NCEP Climate Forecast System Reanalysis (CFSR; Saha et al. 2010), which is generated from the same dynamical core as the GFS data used for the synoptic overview. CFSR implements GFS as its atmospheric model but has the added benefit of better constraining WRF's initial and boundary conditions through additional data assimilation and Earth system model coupling (Saha et al. 2010). As this modification differentiates the WRF configuration used in this study from the near-real-time version, "West-WRF-Exp" is used hereafter to describe the experiments.

The model's fidelity was evaluated relative to radiosonde and dropsonde observations (described in section 2b), NEXRAD radar data, and station meteorological observations. Additionally, an ensemble of 20 simulations with 10 stochastic energy backscatter perturbation (SKEBS) members and

10 varied physics members was generated for this case study to assess the sensitivity of the simulated NCFR to uncertainty in WRF's parameterization schemes and upscale propagating errors from unresolved processes, respectively (e.g., Berner et al. 2011). The physics ensemble consisted of simulations using the WRF single-moment 6-class (Hong et al. 2006) and Morrison (Morrison et al. 2009) microphysics schemes, and the Asymmetric Convection Model (ACM2; Pleim 2007) and Mellor–Yamada–Nakanishi–Niino Level 2.5 (MYNN; Nakanishi and Niino 2004) planetary boundary layer schemes in eight possible combinations. Simulations using the MYNN boundary layer and Thompson Microphysics scheme were also run with the Eta similarity (Janjić 2002) and MYNN surface layer schemes for a total of 10 ensemble members.

Another important source of numerical forecast error, initial conditions, was not accounted for as each ensemble member was forced with identical CFSR initial and boundary conditions. While such an experimental setup may lead to some degree of overconfidence in the predictability of the NCFR (e.g., Durran et al. 2013), the influence of initial condition perturbations on NCFR development was expected to be small in this case given the short integration time, well-developed front, and reanalysis forcing, though this was not tested. A large effort to assess the impact of dropsondes on initial condition error in AR forecasts in global NWP, including for this event, is ongoing as part of AR Recon (Ralph et al. 2020). Note that the sounding observations were assimilated into the real-time GFS as well as the CFSR.

The direct comparison of model profiles against soundings was complicated due to differences in the timing of the NCFR in each West-WRF-Exp simulation, as well as dropsonde drift and the latency between drops. These discrepancies are accounted for in operational data assimilation via background error covariances and observation perturbations, which enable the meaningful calculation of forecast departures from observations (Rodwell et al. 2016). However, because the focus of this work was specifically on evaluating the model's representation of the front in a single case, an optimization approach to identify the profile of temperature, specific humidity, and wind components from the simulated location that best matched each dropsonde on either side of the front was employed to correct spatiotemporal differences [based on equally weighted root-mean-square error (RMSE) and correlation of the full profiles, accounting for sonde drift]. Specifically, the correlation of each dropsonde and model profile pair, and their RMSE, were equally weighted for each variable and their ranked sum was used to determine each ensemble member's transect pair that best represented the observed front. The average displacement of the frontal crossing in the ensemble was roughly 100 km to the southwest of the observed dropsondes that straddled the NCFR (Fig. 7). Because model profiles on the warm (cold) side of the front were generally similar to other nearby profiles on the same side of the front, the results presented here are relatively insensitive. Importantly, this feature-based approach mitigated spatiotemporal discrepancies in evaluating the model's ability to represent the NCFR, which was not possible in unadjusted or uniformly adjusted transects. Although the spatially adjusted data are not suitable for calculating standard forecast skill metrics, general verification statistics were also not a priority given that only a single case was evaluated.

3. Synoptic overview

a. *Event evolution*

A surface low pressure center (i.e., cyclone) with a minimum SLP of ~1004 hPa was located over the eastern North Pacific (Fig. 2a; ~34°N, 132°W) at 1200 UTC 1 February 2019. The large-scale environment containing the cyclone at this time featured many components favorable for quasigeostrophic (QG) forcing for ascent and cyclone deepening. The cyclone was located downstream of a trough at 250 hPa in a dynamically favorable region for QG forcing for ascent proximal to the ascending branch of the ageostrophic circulation inferred by the right-entrance and left-exit regions of two separate jet streaks (e.g., Carlson 1998; Fig. 2b; cyclone location denoted via red dot). The cyclone was also located downstream of a longwave trough at 500 hPa (near ~42°N and 135°W), with an embedded shortwave trough (near 136°W), in a dynamically favorable region for lower-tropospheric geopotential height falls (i.e., cyclone deepening) inferred by positive absolute vorticity advection by the geostrophic wind (e.g., Lin 2007). Temperature and wind at 850 hPa also suggest that the cyclone was forming within the baroclinic zone of an existing cold front associated with a mature cyclone over coastal British Columbia (Fig. 2b). The presence of the cold front in relation to the developing surface low pressure likely provided baroclinic instability to the developing low, thus enhancing the development of the surface cyclone (Shapiro and Keyser 1990). Last, the cyclone contained abundant lower-tropospheric moisture that facilitated QG forcing for ascent by virtue of lowering the effective static stability within a southwest–northeast-oriented AR with a maximum IVT magnitude of ~890 $\mathrm{kg\,m^{-1}\,s^{-1}}$ and a collocated maximum IWV magnitude of ~36 mm at approximately 33°N, 130°W. Combined, these factors led to a SLP decrease within the cyclone of ~20 hPa in the ensuing 24 h (Fig. 3). Coincident with the strengthening of the surface cyclone, the IVT maximum also increased ~200 $\mathrm{kg\,m^{-1}\,s^{-1}}$ within a region encompassing the surface cyclone center and AR core over that time (20°–40°N, 140°–120°W).

The implied presence of QG forcing for ascent described above can be summarized and quantified by the analysis of 700–500 hPa **Q**-vector divergence (e.g., Hoskins et al. 1978; Hoskins and Peddler 1980; Cannon et al. 2018). At 1200 UTC 1 February 2019, the cyclone was collocated with a region of **Q**-vector convergence (negative values) downstream of a shortwave trough at 700-hPa (Fig. 4). The orientation of the **Q** vectors directed toward warmer potential temperatures in the vicinity of the developing cyclone (e.g., ~30°N, 125°W at 1200 UTC 2 February 2019) indicates the presence of lower-tropospheric frontogenesis (Funk 2011). Consequently, the presence of lower-tropospheric frontogenesis and its associated circulations are known to produce banded precipitation structures in conjunction with the release of potential instability, particularly in deepening baroclinic systems (e.g., Markowski and Richardson 2010; Cannon et al. 2018, 2020).

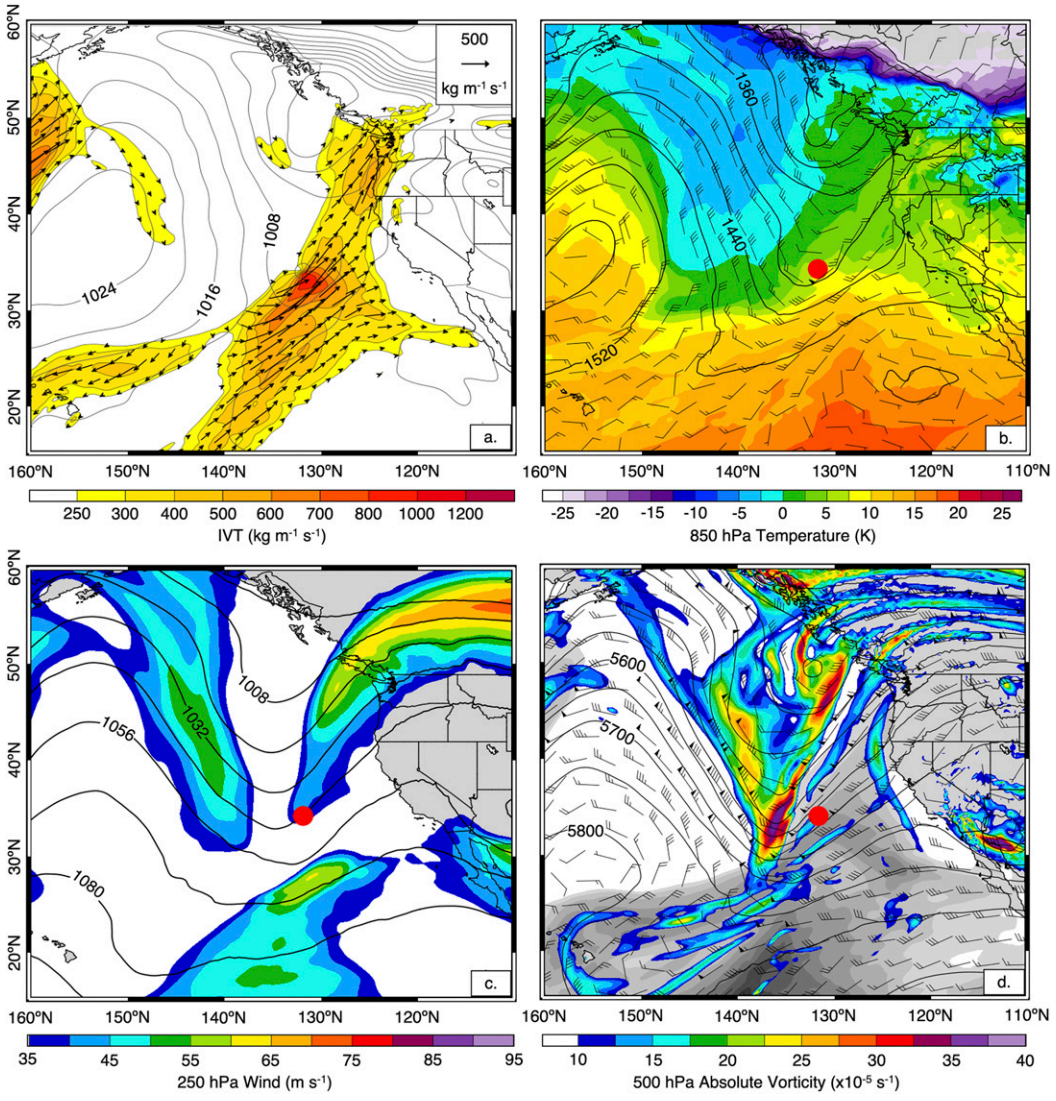

FIG. 2. (a) IVT (filled contours and vectors; kg m^{-1} s^{-1}) and SLP (gray contours; hPa); (b) 850-hPa temperature (filled contours; K), geopotential height (black contours; m), and winds (barb; knots, 1 kt $\approx$ 0.51 m s^{-1}); (c) 250-hPa wind speed (filled contours; m s^{-1}) and geopotential height (black contours; m); and (d) 500-hPa absolute vorticity (filled contours; $\times 10^{-5}$ s^{-1}), geopotential height (black contours; m), IWV (gray shade; mm) and winds (barb; kt) at 1200 UTC 1 Feb 2019. The red dot indicates the center of the surface cyclone.

By 0000 UTC 2 February 2019, the cyclone had deepened 12 hPa in the previous 12 h (Fig. 3) and featured an elongated region of **Q**-vector convergence with multiple maxima along the intensifying cold front (Figs. 4b,c). Over the ensuing 24 h the cyclone continued to propagate eastward and reached a minimum SLP of 984 hPa at 1200 UTC 2 February 2019 (Fig. 3). The **Q**-vector convergence reached a minimum value of $\sim 5 \times 10^{16}$ K m^{-1} s^{-1} at 0000 UTC 3 February 2019 offshore of Southern California, collocated with the landfalling AR [Fig. 4d; the WRF domains used in subsequent analyses (section 4) are shown on this plot for reference]. The following sections illustrate that the associated ageostrophic circulations related to frontogenesis across the AR in the region of **Q**-vector convergence were fundamental to the development of the NCFR. This result suggests that mesoscale processes related to the development and maintenance of the NCFR in this event were linked to quantifiable synoptic-scale processes. Given that these synoptic-scale processes are relatively well resolved in coarse-resolution models consistent with previous studies of NCFRs over Southern California (e.g., Oakley et al. 2018a; Cannon et al. 2018), these results indicate a potential source of forecast guidance at lead times of 3–5 days. In fact, it was GFS and GEFS forecasts of the aforementioned synoptic-scale features, rapid cyclogenesis and frontogenesis that triggered initial flight planning for IOP1 during AR Recon on 28 January 2019.

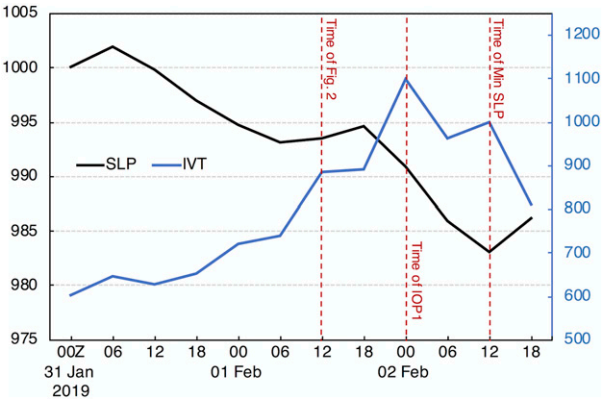

FIG. 3. Time series of minimum SLP (black line; hPa) and maximum IVT (blue line; kg m^{-1} s^{-1}) for the domain 20°–40°N, 140°–120°W. The time of the synoptic analyses in Fig. 2 is marked with a red vertical line at 1200 UTC 1 Feb 2019, as are the time of IOP1 at 0000 UTC 2 Feb 2019 and the time of domain-wide minimum sea level pressure at 1200 UTC 2 Feb 2019.

b. Predictability of synoptic forcing for NCFR development

The rapid cyclogenesis occurred in association with the development of frontogenesis and the observed NCFR on 1–2 February 2019. The GEFS forecasts illustrate that cyclogenesis—inferred from minimum SLP tendency within a region spanning 20°–40°N, 140°–120°W—was forecasted by individual ensemble members up to 5 days in advance (Fig. 5) and was within the ensemble spread 3 days in advance (Fig. 5). Note that the observed minimum SLP of 984 hPa (Fig. 3) was a 99th percentile event for the region based on analysis of 38 years of 6-hourly CFSR analyses. Several of the ensemble members predicted surface cyclones with minimum SLP values $<$ 1000 hPa (97th percentile) in the aforementioned region at 7- and 6-day lead times. The deterministic forecast and ensemble mean both predicted minimum SLP values $<$ 1000 hPa at 4–5-day lead times (Fig. 5). Thus, the relatively coarse GEFS likely accurately simulated the synoptic-scale features associated with rapid cyclogenesis and with enough lead time to consider the possibility of the development of an NCFR. The next section considers the mesoscale predictability applications for the specific event including dedicated high-resolution simulations over the offshore environment.

4. West-WRF-Exp representation of the observed NCFR

The NCFR investigated in this study was observed by the San Diego NEXRAD site as it approached the coastline of San Diego County at 2300 UTC 2 February 2019 (Fig. 6a). The presence of the NCFR was also resolved by the control West-WRF-Exp configuration (Fig. 6b), though finescale details, such as the ''gap and core'' structure and interaction with terrain in the northern portion of the domain, were not well resolved, which has potential implications for hazard warnings. This section evaluates the ensemble West-WRF-Exp configuration's representation of the physical processes leading to the development and evolution of the NCFR, both onshore and offshore using dropsonde and radiosonde observations, and discusses the impact of model uncertainty in the timing, orientation and intensity of the NCFR on hazard forecasting.

Although the NCFR was not observed until it was within 100–200 km of the coastal radars, the conditions that led to its development evolved well offshore of radar coverage (~1000 km west of the Bight; Figs. 2 and 3). This environment included rapid cyclogenesis, a 200 kg m^{-1} s^{-1} increase in IVT over 6 h (Fig. 3), and associated frontogenesis proximal to the conditionally stable cyclone warm sector and AR (Cannon et al. 2018, 2020). Dropsonde measurements from IOP1 (Figs. 1 and 7) enabled an evaluation of the West-WRF-Exp ensemble's representation of physical processes associated with offshore NCFR evolution and maintenance.

Simulated composite reflectivity at the time of IOP1 at 0000 UTC 2 February—24 h after initialization and 23 h preceding the time step shown in Fig. 6—illustrates a well-developed NCFR collocated with a region of strong wind convergence and a 3-K θ_e gradient (Fig. 7a). As in Fig. 6, the general shape and orientation of the NCFR feature was represented with fidelity, though it lacked the defined gap and core structure that is characteristic of observed NCFRs. It is also worth noting that the IVT was strongly influenced by the mesoscale frontal dynamics that drove the NCFR (Fig. 7b).

a. Comparison of WRF and sounding observations

A qualitative comparison between the dropsondes and the spatially adjusted West-WRF-Exp ensemble profiles suggests that the relative magnitude of the winds and water vapor were similar between observations and model simulation (Fig. 8). The ensemble configuration also adequately represented the observed frontal structure, as illustrated by the simulated horizontal wind shear and reduction in both wind speed and water vapor in the model after the frontal passage (Fig. 8). The ensemble also demonstrated that the scale of the differences between pre- and postfrontal soundings was much larger than the uncertainty in the simulation of those features.

Radiosondes launched from SIO (see location on Fig. 6) before and after the passage of the NCFR were also used to evaluate the ensemble's ability to maintain the physical processes relevant to NCFR evolution throughout the 48-h simulation. Qualitative comparisons between the best-matched simulated ensemble profiles from 2300 UTC 2 February 2019 and sounding data from 2242 to 2317 UTC (Fig. 9) indicated that the simulated profiles of temperature (Fig. 9a) vapor mixing ratio (Fig. 9b), wind speed (Fig. 9c), water vapor flux (Fig. 9d), and wind direction (Fig. 9e) were still representative of the observed NCFR 2 days beyond model initialization. However, the water vapor mixing ratio profiles were notably different between ensemble simulations and the radiosondes in both the warm and cold sectors (perhaps due to issues in representing the rapid evolution of the moisture budget in a region of strong convergence and precipitation), and the prefrontal winds near 0.5-km elevation were underestimated in nearly all ensemble members.

The ensemble-based approach to accounting for model uncertainty, and the pre and postfrontal wind and humidity differences of similar magnitude as the dropsonde and radiosonde observations, suggest that the West-WRF-Exp configuration

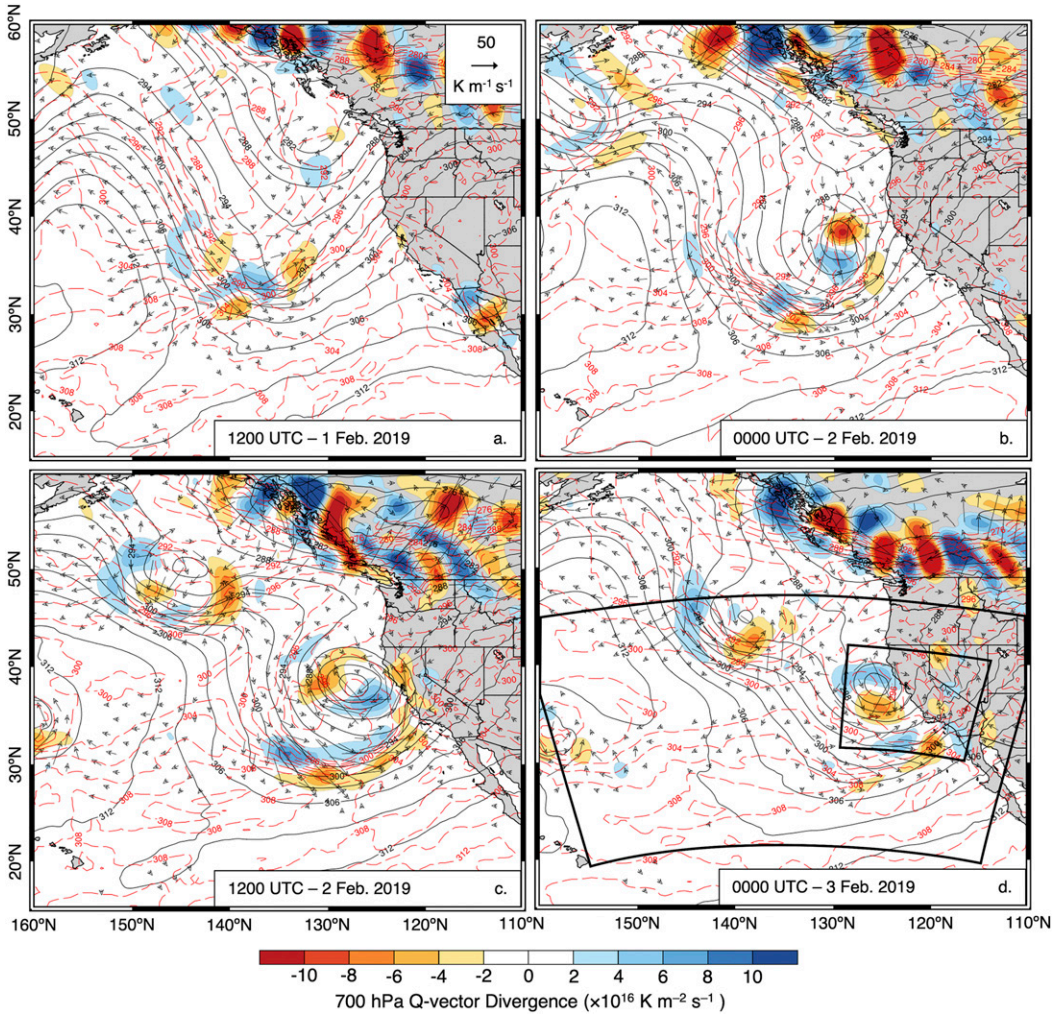

FIG. 4. 700 hPa **Q**-vector divergence (filled contours), geopotential height (solid black contours; m), potential temperature (dashed red contours; K), and temperature advection (vectors; K s^{-1}) every 12 h from (a) 1200 UTC 1 Feb 2019 to (d) 0000 UTC 3 Feb 2019. The WRF 9-km (outer) and 3-km (inner) domains used in subsequent analyses are also plotted in black in (d) for reference.

adequately simulated the frontal structure that was fundamental to NCFR development, even in the absence of assimilated radar data [e.g., as in the operational High-Resolution Rapid Refresh (HRRR) model, which also generated an NCFR in each of its 18 forecast initializations preceding this event's landfall (not shown)]. However, given the 3-km spatial resolution, which can only fully resolve meteorological features on the order of ~15–25 km (Warner 2011) and parameterized precipitation, it was not necessarily expected that the WRF configuration used here would replicate the detailed structure of the NCFR, as inferred from Fig. 6 and the temperature and moisture departures in Figs. 9a and 9b—this point is further discussed in the following subsection.

b. West-WRF-Exp simulation of NCFR timing and location

While all West-WRF-Exp ensemble simulations reproduced the development of the observed NCFR and reasonably represented observed profiles of moisture and wind (Figs. 6–9), the representation of the NCFR's propagation, structure and intensity varied across ensemble members. Additionally, the small-scale gap and core structures within the NCFR were not simulated (Fig. 10). The observed NCFR reached the longitude of Los Angeles (~118°W) at 2100 UTC 2 February (Fig. 9a), corresponding to hour 45 of the ensemble forecasts that were initialized at 0000 UTC 1 February. The 45 h since initialization were sufficient for the model perturbations to result in ensemble dispersion, though most ensemble members' NCFRs were within 100 km of one another.

Each ensemble member produced an NCFR, though the structure and orientation of the region with simulated reflectivity > 40 dBZ varied across members (Fig. 10a). The ensemble mean NCFR position within the California Bight, identified by the band of maximum reflectivity > 40 dBZ in each member, was at approximately the same longitude as the observed NCFR at that

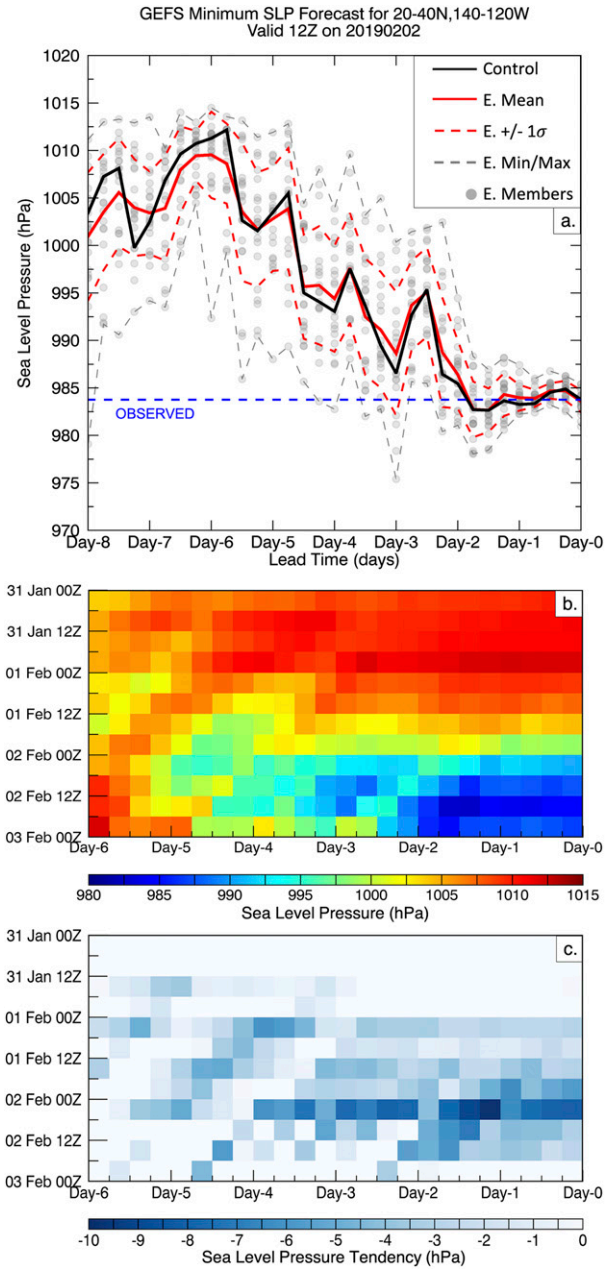

FIG. 5. (a) Individual GEFS member SLP minima for the region 20°–40°N, 140°–120°W according to forecast lead time valid at 1200 UTC 2 Feb 2019. The ensemble control, mean, spread, minimum, and maximum are identified, and the observed value at the day-0 valid time is indicated by a blue dashed line. (b) Ensemble mean SLP minima for the same region and (c) their rate of change over 6-h increments for each forecast lead time (x axis) at each forecast valid time between 0000 UTC 31 Jan 2019 and 0000 UTC 3 Feb 2019 (y axis).

time (not shown), the ensemble spread was approximately ±0.5° longitude (±50 km), and the maximum and minimum longitudes were ~120° and ~117°W, respectively (Fig. 10a). The ensemble spread was largest among the 10 SKEBS members and smallest among the multiphysics members; the former introduced large differences in the timing of the front.

A composite transect of ensemble reflectivity and circulation, with each member's transect centered and normalized about its maximum dBZ profile before compositing, is shown in Fig. 10b. This composite illustrates the model configuration's robustness in simulating the key physical processes that define NCFRs in theory and observation (e.g., Hobbs 1978; Hobbs and Persson 1982; Jorgensen et al. 2003), despite uncertainty in the location, timing and intensity of the resultant NCFR. Several features characteristic of NCFRs that were captured in the model simulations include the following:

- NCFRs are commonly associated with the presence of a strong low-level jet (LLJ) (Koch and Kocin 1991): Fig. 9b illustrates that the West-WRF-Exp ensemble mean wind and vapor transport profiles also featured a LLJ, though the maximum observed wind speed of 30 m s^{-1} at 0.5-km altitude is slightly higher than the ensemble spread.
- NCFRs are typically associated with a sharp defined cold front that can be identified by a >2-K discontinuity in the potential temperature θ field; Browning 1986): Figs. 7a and 10b illustrate a 3-K θ_e gradient in simulations.
- Convection in NCFRs is initiated by convergence and the release of conditional instability at the frontal boundary between westerly postfrontal flow and southeasterly prefrontal flow (Locatelli et al. 1995; Jorgensen et al. 2003; Persson et al. 2005): Fig. 10b illustrates convergent low-level flow at the frontal boundary.
- NCFRs often lack conditional convective instability (Houze et al. 1976; Jorgensen et al. 2003): Thermodynamic profiles illustrate 0 J kg^{-1} of CAPE in pre-NCFR soundings, dropsondes and West-WRF-Exp profiles (not shown).
- NCFRs are ~2–6 km deep (Houze et al. 1976; Browning 1986; Jorgensen et al. 2003): Fig. 10b illustrates that the observed NCFR in this case study extends to 2–3 km, inferred from the vertical extent of >40 dBZ reflectivity and gradients of wind and θ_e. The simulated NCFR depth is in agreement with vertically interpolated NEXRAD reflectivity (not shown). This limited vertical extent creates an additional challenge for NCFR observation via radar, which tends to overshoot the most intense echoes with increasing distance (Jorgensen et al. 2003).

The fact that each of the primary components of canonical NCFR development were identified in the ensemble composite is encouraging for the use of mesoscale numerical weather prediction (NWP) in forecasting these events. However, the ensemble analyses also highlight sensitivity in timing of the simulated NCFR to uncertainty in model physics and upscale propagating errors (in addition to initial condition error, which was not accounted for here). This uncertainty, along with the inadequate representation of small-scale structures (i.e., gaps and cores) that create spatial variability in the precipitation intensity and duration across relatively small spatial scales over Southern California (e.g., Figs. 5b, 7a, and 9a), limit the predictability of NCFR impacts. Future improvements of the representation of the spatiotemporal variability of NCFRs at small scales (e.g., via improved model horizontal resolution,

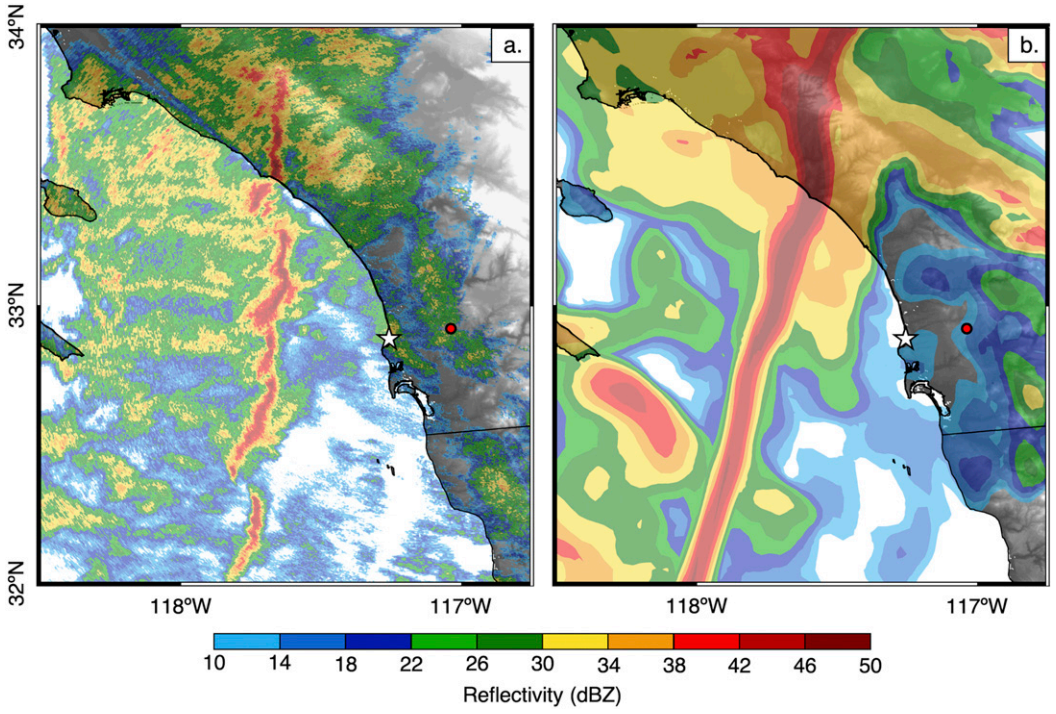

FIG. 6. (a) NEXRAD base (0.46°) radar reflectivity at 2200 UTC and (b) West-WRF-Exp simulated composite reflectivity at 2300 UTC 2 Feb 2019 from the control simulation. The control simulation NCFR lagged behind the observed NCFR by ~1 h. The San Diego NEXRAD site is marked by a red circle, and the radiosonde launch location at SIO is denoted by a white star.

additional physics testing, and more thorough ensemble development) would augment hazard precipitation forecasting, especially at scales on the order of several kilometers (e.g., a burn area, a small watershed that is prone to flash flooding, or local inflow to regional reservoirs).

5. Precipitation characteristics of the NCFR event

The maximum composite reflectivity observation from all ~5-min scans of the San Diego NEXRAD (KNKX) over a 3-h window between 2100 and 2355 UTC 2 February 2019 shows the continued propagation of the NCFR across the Bight (Fig. 11). Compared to WRF simulated reflectivity (output at hourly resolution), the observed NCFR exhibited a characteristic gap and core structure that persisted through the entire period, with individual cells being advected northeastward by the geostrophic circulation as the cold front and NCFR propagated southeastward. The rapidly evolving nature of the "core" regions within NCFRs increases the likelihood of false alarm cases in which NCFR passage is predicted to occur, and does, but hazardous precipitation does not. In such events the intensity, location, and timing of the overall NCFR can be well forecast, though individual locations under subsequent hazard warnings may not be impacted due to the position of the location in a light precipitation "gap" of the NCFR while adjacent areas experienced heavy precipitation associated with a "core." Additionally, the orientation and motion of the NCFR, as well as its interaction with terrain (Viale et al. 2013), may impact precipitation intensity and duration over a given area (Doswell et al. 1996). Such was the case with the Holy Fire burn area during this event (Fig. 11). Propagation of the NCFR was inhibited by the ~1000–1700-m Santa Ana Mountains immediately southwest of the burn area, resulting in more moderate precipitation intensities than observed at locations upstream and farther south of the mountains. It is worth noting that NEXRAD assimilation (e.g., in the HRRR operational system) may improve the performance of the model in representing gap and core structures, though that topic is left for future research.

The spatial variability observed in the radar is also represented in the regional rain gauge network. The Oceanside rain gauge recorded a maximum 5-min precipitation accumulation of 5.7 mm and a maximum 15-min precipitation accumulation of 12.0 mm coincident with the passage of the NCFR—this 15-min accumulation represents one-third of the event total over a 9-h period. In contrast, other stations in the vicinity of the Oceanside gauge (e.g., San Onofre, Carlsbad, and Encinitas) did not observe similar 5- or 15-min accumulations as no NCFR core features affected those areas (Figs. 11 and 12). The only other available station that observed heavy precipitation was Bonsall (east of Oceanside), which was affected by the same NCFR core as Oceanside approximately 20 min later. The considerable spatial variability in precipitation intensities illustrates how nowcasting event impacts by translating real-time radar and station observations to a putative position several hours later can be a difficult problem for regional forecast offices. Furthermore, given radar limitations in this region, such as radar elevation, beam broadening, blocking,

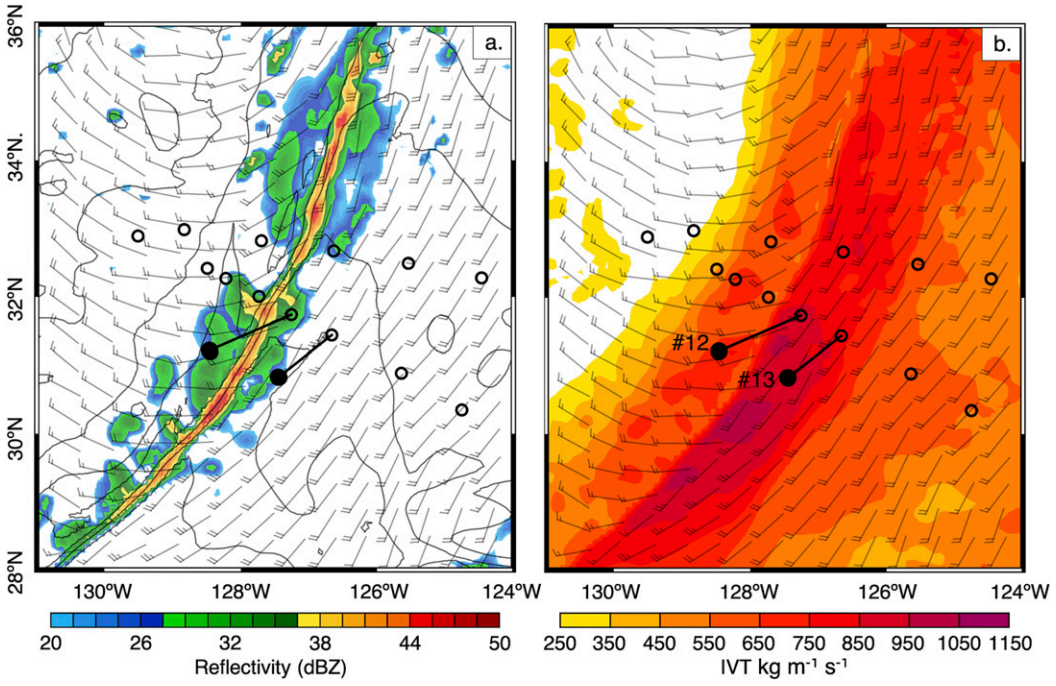

FIG. 7. (a) West-WRF-Exp simulated composite reflectivity (color fill; dBZ), 850-hPa winds (barbs; m s^{-1}), and surface θ_e (contours; K) at 0000 UTC 2 Feb 2019, corresponding to the approximate time of AR Recon dropsonde releases across the NCFR. Open circles indicate the location of dropsonde at their release, and the connected black circles indicate the location of the best-matched WRF profiles resulting from the optimization approach (drops 12 and 13 straddle the front) and (b) dropsonde circles as in (a), WRF IVT (color fill; kg m^{-1} s^{-1}), and 850 hPa winds (barbs; m s^{-1}).

overshoot, and unconstrained reflectivity to rain rate (Z–R) relationships (National Research Council 2005; Martner et al. 2008), it is often the case that large discrepancies exist between precipitation gauges and radar estimates, which degrades nowcast confidence and the ability to generate actionable information for hazard mitigation.

6. Conclusions

Recent research to investigate the meteorological origins of short-duration, high-intensity precipitation events in Southern California has identified narrow cold-frontal rainbands (NCFR) as a common mechanism for generating hazard precipitation (Oakley et al. 2017, 2018a; Cannon et al. 2018). Regionally,

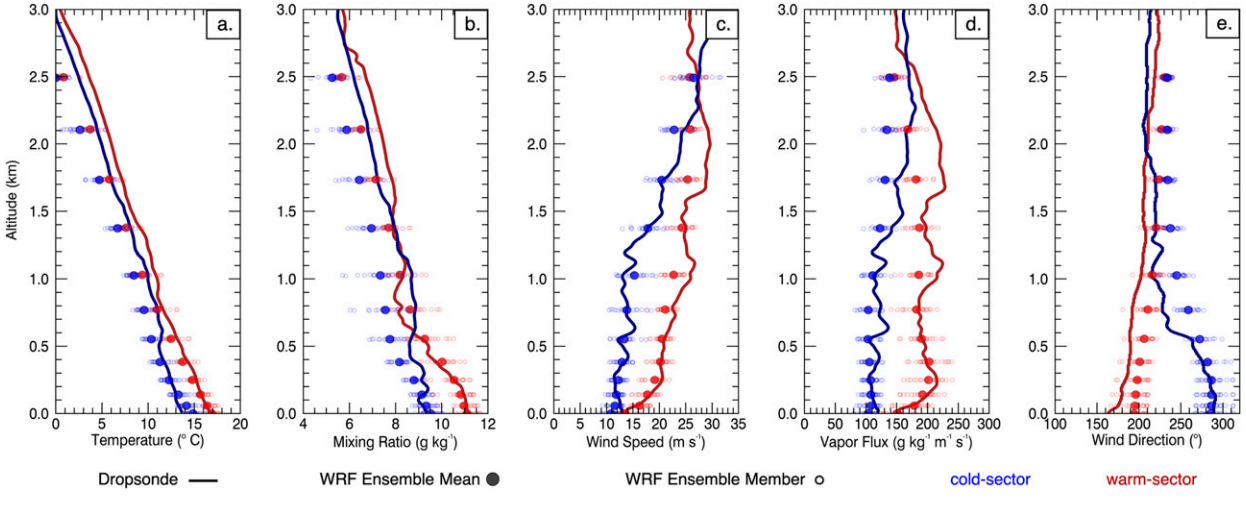

FIG. 8. Dropsondes 12 (in the cold sector behind the front; blue line) and 13 (in the warm sector ahead of the front; red line) and the corresponding West-WRF-Exp ensemble member (small open circles) and mean (large filled circle) profiles for (a) temperature, (b) water vapor mixing ratio, (c) wind speed, (d) vapor flux, and (e) wind direction, plotted on model levels.

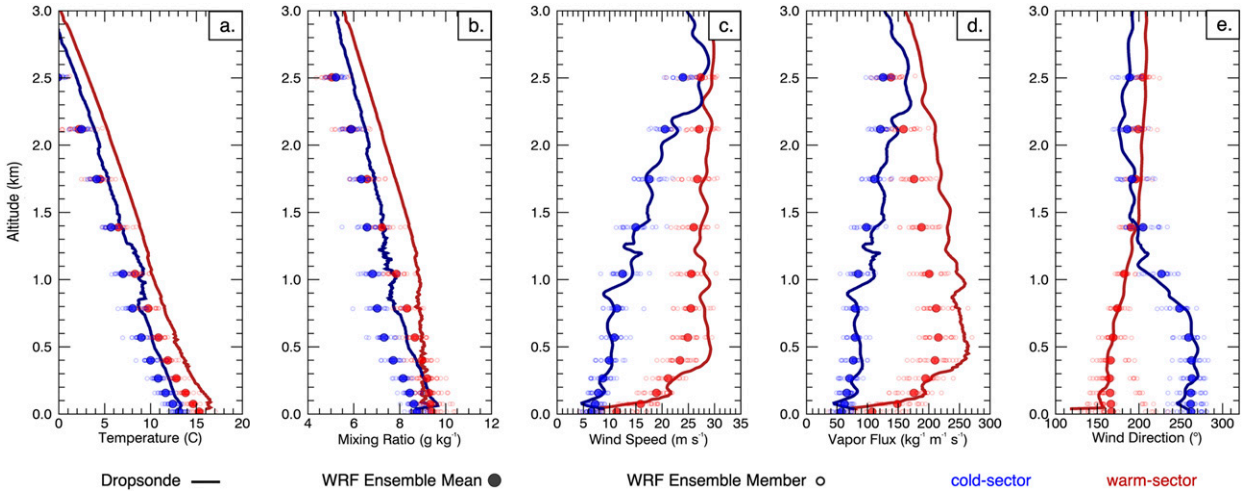

FIG. 9. Radiosonde profiles of (a) temperature, (b) water vapor mixing ratio, (c) wind speed, (d), vapor flux, and (e) wind direction. Corresponding West-WRF-Exp ensemble members (small open circles) and mean (large filled circle) from 2242 UTC (red), in the warm sector ahead of the NCFR passage, and from 2317 UTC (blue), in the cold sector immediately after NCFR passage on 2 Feb 2019, are also shown on model levels.

a lead time of at least 18 h is necessary to provide county officials with sufficient time to conduct evacuations in advance of flash flooding and debris flows associated with high-intensity precipitation (NWS San Diego 2018, personal communication). The challenge of producing meaningful, actionable warnings considering that real-time observational networks typically do not provide sufficient lead times, combined with a need to be sensitive to false alarms and evacuation fatigue (e.g., Gomberg et al. 2018; Kolden and Henson 2019) provides motivation for investigating the predictability of Southern California hazard precipitation across spatiotemporal scales. Here, we identified the synoptic, mesoscale, and local-scale meteorological processes that developed and maintained an NCFR, as well as the predictability of the feature, using observations from the AR Recon field campaign, the existing meteorological network, and NWP output at various grid scales and lead times.

With respect to the predictability of NCFRs, we determined that

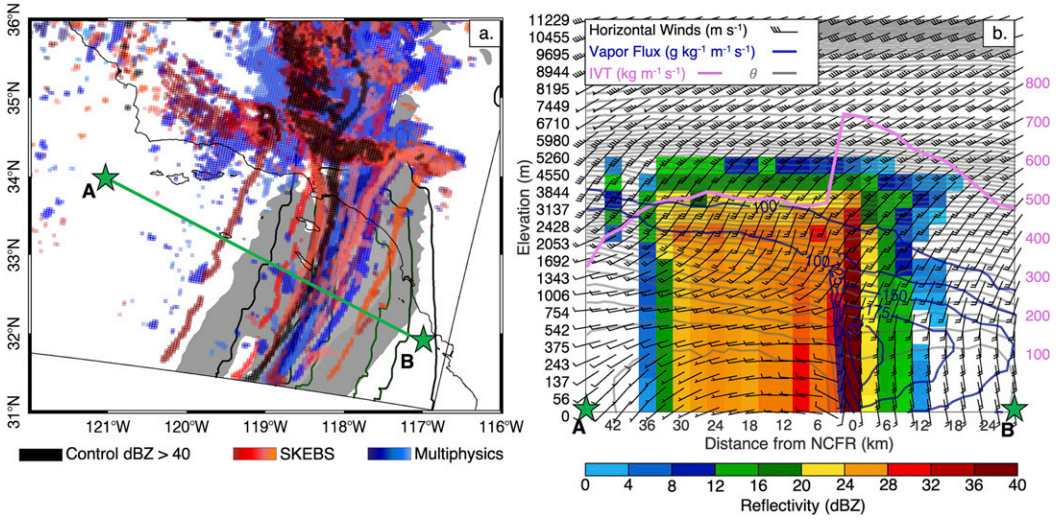

FIG. 10. (a) West-WRF-Exp composite reflectivity > 40 dBZ for each SKEBS ensemble member (red shades) and each multiphysics ensemble member (blue shades) over WRF IVT > 500 kg m^{-1} s^{-1} from the control run (gray shading). The green line in (a) identifies the location of the transect shown in (b). (b) Transect of composite ensemble reflectivity (color), water vapor flux (blue contour), potential temperature (gray contour), and horizontal winds (barbs) across the green line in (a). The mean was taken after centering each member upon its reflectivity maximum to highlight NCFR processes irrespective of spatiotemporal uncertainty.

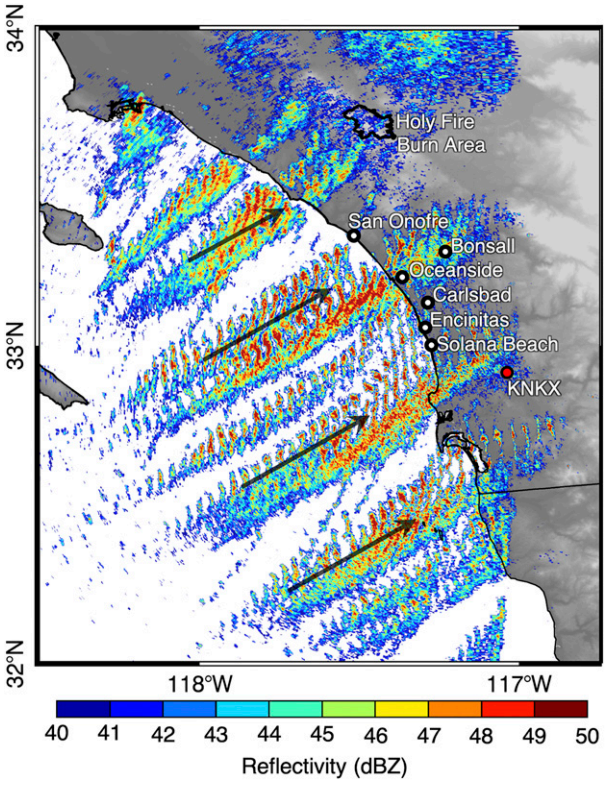

FIG. 11. NEXRAD reflectivity maximum for each ~5-min base-elevation scan composited for all scans between 2100 and 2355 UTC 2 Feb 2019 (color fill) over topography (gray shade). The San Diego NEXRAD site (KNKX) is identified by the red circle. The Holy Fire burn area is indicated by the black contour. ALERT network rain gauges are denoted by circles. The black lines denote the advection of NCFR cores northeastward over the time period, which is oblique to the cold front and NCFR's east-southeastward propagation.

- The physical processes driving NCFR development at the mesoscale in the 2 February 2019 case studied here were linked to quantifiable synoptic-scale forcing that were well-resolved in coarse-resolution models with minimal timing uncertainty in this case, indicating a potential source of forecast guidance at long lead times.
- Large-scale signatures of a dynamically active event, such as rapid cyclogenesis and cold frontogenesis, were apparent along the observed NCFR. Identification of such features in operational forecast systems (e.g., GFS) may act as an indicator for increased likelihood of NCFR development in an approaching system at lead times of several days that are sufficient to allocate additional effort and resources to mesoscale predictability applications (e.g., Warn-on-Forecast; Stensrud et al. 2009).
- Mesoscale NWP models are capable of simulating the development of NCFRs and their driving meteorology ahead of landfall, even in the absence of radar data assimilation.
- The development of the NCFR in a mesoscale model was insensitive to model physics or subgrid-scale errors, as all 21 ensemble members generated intense banded precipitation along the cold front over the Southern California Bight in the event studied, though the timing of its progression and landfall varied and the ensemble mean was delayed by 1 h relative to the observed NCFR at the end of the 48-h simulation period.

Knowledge of the above phenomenon supports increased forecaster confidence at multiday lead times ahead of future NCFR events. Though indicators of predictability and usefulness of NWP at large- to mesoscales were apparent in this particular event, NCFRs are dynamic and evolving features with numerous forecast challenges as well as opportunities for improving their predictability at local scales, such as

- Improvement in operational mesoscale model simulations with regard to gap and core structure is needed to aid decision-making over localized high-risk areas (e.g., to support evacuation planning near recent burn areas).
- Improved ability to assess rainfall intensities, as station data in the area of complex terrain studied here are sparse and radar faces issues of beam blockage, overshoot, and Z–R uncertainty, which collectively reduce reliability in estimating rainfall rates and degrade the ability to generate actionable information for hazard mitigation.

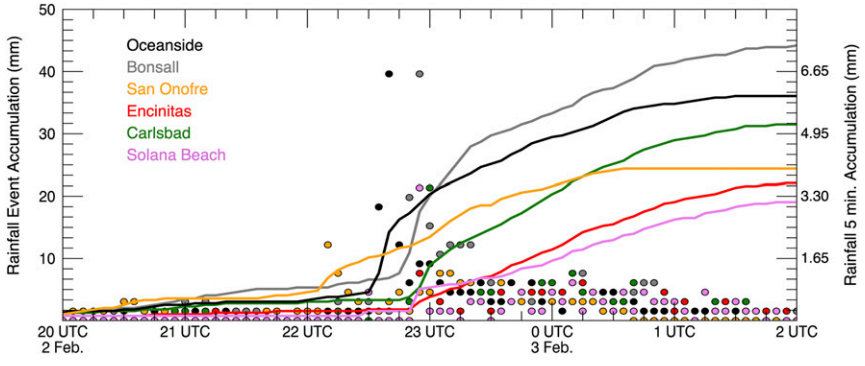

FIG. 12. Accumulated event precipitation starting at 2000 UTC 2 Feb 2019 (line) and 5-min precipitation accumulation (circles) at coastal ALERT gauge stations in the San Diego County network between 2000 UTC 2 Feb and 0200 UTC 3 Feb 2019.

Continued work will focus on evaluating mesoscale model uncertainty in short-range NCFR forecasts over point locations, including from the HRRR, which assimilates radar observations and thus may propagate an observed NCFR with more fidelity, and using higher-resolution simulations (e.g., a 1-km nest). Additionally, the Center for Western Weather and Water Extremes at SIO has sited multiple disdrometers, profiling radars, and radiosonde launch locations in Southern California to sample extreme events and provide observations that support ongoing forecast model development.

Moving forward, it is necessary to extend the methodology implemented in this case study to a larger sample of NCFR events. Here, consistency with previous research and several other recent events that were monitored in near–real time lend confidence to our results, but it should be noted that a formal quantification of NWP skill in NCFR events is unknown to the authors. Current efforts to address these deficiencies include the creation of a climatology of NCFRs in the Southern California Bight, evaluation of NCFR representation in the operational HRRR as well as a recently generated 30-yr West-WRF reforecast, and ensemble simulation of a large sample of NCFRs for more thorough sensitivity analysis. Furthermore, it will be necessary to evaluate the potential for false alarms—events in which the synoptic and/or mesoscale conditions favor NCFR development, but the forecasted feature fails to verify—to define and communicate the uncertainty of this approach. As short-duration, high-intensity precipitation and flash floods are likely to increase in future climate (Westra et al. 2014; Modrick and Georgakakos 2015; Prein et al. 2017), there is increasing need to better understand, model, forecast, and message about extreme precipitation producing features such as NCFRs.

Acknowledgments. This research was supported by the California Department of Water Resources and the U.S. Army Corps of Engineers (USACE) as part of Forecast Informed Reservoir Operations (FIRO) under Grant W912HZ-15-2-0019. Funding was also provided by the Orange County Water District and in part by the National Oceanic and Atmospheric Administration (NOAA) Collaborative Science, Technology, and Applied Research (CSTAR) Program under Grant NA19NWS4680004. The NCEP data used in this research were developed by the NOAA. The WRF Model was made available by the National Center for Atmospheric Research, sponsored by the National Science Foundation (NSF). West-WRF-Exp simulations were performed on the San Diego Supercomputing Center's COMET resource through NSF XSEDE Award ATM150010. AR Recon observations were made possible by the support of the U.S. Air Force 53rd Weather Reconnaissance Squadron.

REFERENCES

American Meteorological Society, 2012: Rain. Glossary of Meteorology. Accessed 3 October 2019, http://glossary.ametsoc.org/wiki/Rain.

Berner, J., S. Ha, J. P. Hacker, A. Fournier, and C. Snyder, 2011: Model uncertainty in a mesoscale ensemble prediction system: Stochastic versus multiphysics representations. *Mon. Wea. Rev.*, **139**, 1972–1995, https://doi.org/10.1175/2010MWR3595.1.

Blier, W., 2003: An examination of an intense land-falling narrow cold frontal rainband using the Weather Event Simulator (WES). National Weather Service Western Region Technical Attachments, accessed 3 October 2019, 9 pp., https://www.weather.gov/media/wrh/online_publications/talite/talite0313.pdf.

Browning, K. A., 1986: Conceptual models of precipitation systems. *Wea. Forecasting*, **1**, 23–41, https://doi.org/10.1175/1520-0434(1986)001<0023:CMOPS>2.0.CO;2.

Cannon, F., C. W. Hecht, J. M. Cordeira, and F. M. Ralph, 2018: Synoptic and mesoscale forcing of Southern California extreme precipitation. *J. Geophys. Res. Atmos.*, **123**, 13 714–13 730, https://doi.org/10.1029/2018JD029045.

——, J. M. Cordeira, C. W. Hecht, J. R. Norris, A. Michaelis, R. Demirdjian, and F. M. Ralph, 2020: GPM satellite radar observations of precipitation mechanism in atmospheric rivers. *Mon. Wea. Rev.*, **148**, 1449–1463, https://doi.org/10.1175/MWR-D-19-0278.1.

Cannon, S. H., J. E. Gartner, R. C. Wilson, J. C. Bowers, and J. L. Laber, 2008: Storm rainfall conditions for floods and debris flows from recently burned areas in southwestern Colorado and southern California. *Geomorphology*, **96**, 250–269, https://doi.org/10.1016/j.geomorph.2007.03.019.

Carlson, T. N., 1998: *Mid-Latitude Weather Systems*. Amer. Meteor. Soc., 507 pp.

CBS Los Angeles, 2019: Storm brings heavy rain and high winds, shuts down 101 freeway and PCH. *KCAL 9 CBS Los Angeles*, accessed 21 November 2019, https://losangeles.cbslocal.com/2019/02/02/stormy-saturday-socal/.

Cordeira, J. M., F. M. Ralph, A. Martin, N. Gaggini, J. R. Spackman, P. J. Neiman, J. J. Rutz, and R. Pierce, 2017: Forecasting atmospheric rivers during CalWater 2015. *Bull. Amer. Meteor. Soc.*, **98**, 449–459, https://doi.org/10.1175/BAMS-D-15-00245.1.

County of San Diego, 2019: San Diego County Rainfall and Stream Level Information System. Accessed 5 June 2019, https://sandiego.onerain.com/.

Doswell, C. A., H. E. Brooks, and R. A. Maddox, 1996: Flash flood forecasting: An ingredients-based methodology. *Wea. Forecasting*, **11**, 560–581, https://doi.org/10.1175/1520-0434(1996)011<0560:FFFAIB>2.0.CO;2.

Durran, D. R., P. A. Reinecke, and J. D. Doyle, 2013: Large-scale errors and mesoscale predictability in Pacific Northwest snowstorms. *J. Atmos. Sci.*, **70**, 1470–1487, https://doi.org/10.1175/JAS-D-12-0202.1.

Funk, T., 2011: A practical, basic guide to quasi-geostrophic theory, response to geostrophic deformation, ageostrophc motion and jet streaks. National Weather Service, Louisville, KY, 26 pp., https://www.weather.gov/media/lmk/soo/QG_Theory_Review.pdf.

Gatzen, C., 2011: A 10-year climatology of cold-season narrow cold-frontal rainbands in Germany. *Atmos. Res.*, **100**, 366–370, https://doi.org/10.1016/j.atmosres.2010.09.018.

Gomberg, D., J. Laber, and E. Boldt, 2018: Forecast and warning of the Montecito debris flow event—January 9, 2018. *Workshop on Assessing Meteorological Events Leading to the Montecito Debris Flow*, Santa Barbara, CA, University of California, Santa Barbara.

Grell, G. A., and D. Dévényi, 2002: A generalized approach to parameterizing convection combining ensemble and data assimilation techniques. *Geophys. Res. Lett.*, **29**, 1693, https://doi.org/10.1029/2002GL015311.

Hobbs, P. V., 1978: Organization and structure of clouds and precipitation on the mesoscale and microscale in cyclonic storms. *Rev. Geophys. Space Phys.*, **16**, 741–755, https://doi.org/10.1029/RG016i004p00741.

——, and P. O. G. Persson, 1982: The mesoscale and microscale structure and organization of clouds and precipitation in midlatitude cyclones. Part V: The substructure of narrow cold-frontal rainbands. *J. Atmos. Sci.*, **39**, 280–295, https://doi.org/10.1175/1520-0469(1982)039<0280:TMAMSA>2.0.CO;2.

Hong, S., Y. Noh, and J. Dudhia, 2006: A new vertical diffusion package with an explicit treatment of entrainment processes. *Mon. Wea. Rev.*, **134**, 2318–2341, https://doi.org/10.1175/MWR3199.1.

Hoskins, B. J., and M. A. Peddler, 1980: The diagnosis of middle latitude synoptic development. *Quart. J. Roy. Meteor. Soc.*, **106**, 707–719, https://doi.org/10.1002/qj.49710645004.

——, I. Draghici, and H. C. Davies, 1978: A new look at the ω-equation. *Quart. J. Roy. Meteor. Soc.*, **104**, 31–38, https://doi.org/10.1002/qj.49710443903.

Houze, R. A., P. V. Hobbs, K. R. Biswas, and W. M. Davis, 1976: Mesoscale rainbands in extratropical cyclones. *Mon. Wea. Rev.*, **104**, 868–878, https://doi.org/10.1175/1520-0493(1976)104<0868:MRIEC>2.0.CO;2.

——, and Coauthors, 2017: The Olympic Mountains Experiment (OLYMPEX). *Bull. Amer. Meteor. Soc.*, **98**, 2167–2188, https://doi.org/10.1175/BAMS-D-16-0182.1.

Janjić, Z. I., 2002: Nonsingular implementation of the Mellor–Yamada Level 2.5 scheme in the NCEP Meso model. NCEP Office Note 437, 61 pp.

Jiménez, P. A., J. Dudhia, J. F. González-Rouco, J. Navarro, J. P. Montávez, and E. García-Bustamante, 2012: A revised scheme for the WRF surface layer formulation. *Mon. Wea. Rev.*, **140**, 898–918, https://doi.org/10.1175/MWR-D-11-00056.1.

Jorgensen, D. P., Z. Pu, P. O. Persson, and W. Tao, 2003: Variations associated with cores and gaps of a Pacific narrow cold frontal rainband. *Mon. Wea. Rev.*, **131**, 2705–2729, https://doi.org/10.1175/1520-0493(2003)131<2705:VAWCAG>2.0.CO;2.

Kean, J. W., D. M. Staley, and S. H. Cannon, 2011: In situ measurements of post-fire debris flows in southern California: Comparisons of the timing and magnitude of 24 debris-flow events with rainfall and soil moisture conditions. *J. Geophys. Res.*, **116**, F04019, https://doi.org/10.1029/2011JF002005.

Koch, S. E., and P. J. Kocin, 1991: Frontal contraction processes leading to the formation of an intense narrow rainband. *Meteor. Atmos. Phys.*, **46**, 123–154, https://doi.org/10.1007/BF01027339.

Kolden, C. A., and C. Henson, 2019: A socio-ecological approach to mitigating wildfire vulnerability in the Wildland urban interface: A case study from the 2017 Thomas fire. *Fire*, **2**, 9, https://doi.org/10.3390/fire2010009.

Lin, Y. L., 2007: *Mesoscale Dynamics*. Cambridge University Press, 630 pp.

Locatelli, J. D., J. E. Martin, and P. V. Hobbs, 1995: Development and propagation of precipitation cores on cold fronts. *Atmos. Res.*, **38**, 177–206, https://doi.org/10.1016/0169-8095(94)00093-S.

Markowski, P., and Y. Richardson, 2010: *Mesoscale Meteorology in Midlatitudes*. Wiley Blackwell, 407 pp.

Martin, A., F. M. Ralph, R. Demirdjian, L. DeHaan, R. Weihs, J. Helly, D. Reynolds, and S. Iacobellis, 2018: Evaluation of atmospheric river predictions by the WRF Model using aircraft and regional mesonet observations of orographic precipitation and its forcing. *J. Hydrometeor.*, **19**, 1097–1113, https://doi.org/10.1175/JHM-D-17-0098.1.

Martner, E. B., S. E. Yuter, A. B. White, S. Y. Matrosov, D. E. Kingsmill, and F. M. Ralph, 2008: Raindrop size distributions and rain characteristics in California coastal rainfall for periods without a radar bright band. *J. Hydrometeor.*, **9**, 408–425, https://doi.org/10.1175/2007JHM924.1.

Mlawer, E. J., S. J. Taubman, P. D. Brown, M. J. Iacono, and S. A. Clough, 1997: Radiative transfer for inhomogeneous atmospheres: RRTM, a validated correlated-k model for the longwave. *J. Geophys. Res.*, **102**, 16 663–16 682, https://doi.org/10.1029/97JD00237.

Modrick, T. M., and K. P. Georgakakos, 2015: The character and causes of flash flood occurrence changes in mountainous small basins of Southern California under projected climatic change. *J. Hydrol. Reg. Stud.*, **3**, 312–336, https://doi.org/10.1016/j.ejrh.2015.02.003.

Morrison, H., G. Thompson, and V. Tatarskii, 2009: Impact of cloud microphysics on the development of trailing stratiform precipitation in a simulated squall line: Comparison of one- and two-moment schemes. *Mon. Wea. Rev.*, **137**, 991–1007, https://doi.org/10.1175/2008MWR2556.1.

Nakanishi, M., and H. Niino, 2004: An improved Mellor–Yamada Level-3 model with condensation physics: Its design and verification. *Bound.-Layer Meteor.*, **112**, 1–31, https://doi.org/10.1023/B:BOUN.0000020164.04146.98.

National Research Council, 2005: *Flash Flood Forecasting over Complex Terrain: With an Assessment of the Sulphur Mountain NEXRAD in Southern California*. The National Academies Press, 206 pp., https://doi.org/10.17226/11128

Neiman, P. J., F. Martin Ralph, P. O. Persson, A. B. White, D. P. Jorgensen, and D. E. Kingsmill, 2004: Modification of fronts and precipitation by coastal blocking during an intense landfalling winter storm in southern California: Observations during CALJET. *Mon. Wea. Rev.*, **132**, 242–273, https://doi.org/10.1175/1520-0493(2004)132<0242:MOFAPB>2.0.CO;2.

NOAA, 1991: NOAA Next Generation Radar (NEXRAD) Level 2 Base Data [Reflectivity]. NOAA/National Centers for Environmental Information, NOAA/National Weather Service (NWS) Radar Operations Center, accessed 2019, 2020, https://doi.org/10.7289/V5W9574V.

Norris, J., G. Vaughan, and D. M. Schultz, 2017: Variability of precipitation along cold fronts in idealized baroclinic waves. *Mon. Wea. Rev.*, **145**, 2971–2992, https://doi.org/10.1175/MWR-D-16-0409.1.

Oakley, N. S., J. T. Lancaster, M. L. Kaplan, and F. M. Ralph, 2017: Synoptic conditions associated with cool season post-fire debris flows in the Transverse Ranges of southern California. *Nat. Hazards*, **88**, 327–354, https://doi.org/10.1007/s11069-017-2867-6.

——, F. Cannon, R. Munroe, J. T. Lancaster, D. Gomberg, and F. M. Ralph, 2018a: Brief communication: Meteorological and climatological conditions associated with the 9 January 2018 post-fire debris flows in Montecito and Carpinteria, California, USA. *Nat. Hazards Earth Syst. Sci.*, **18**, 3037–3043, https://doi.org/10.5194/nhess-18-3037-2018.

——, J. T. Lancaster, B. J. Hatchett, J. Stock, F. M. Ralph, S. Roj, and S. Lukashov, 2018b: A 22-year climatology of cool season hourly precipitation thresholds conducive to shallow landslides in California. *Earth Interact.*, **22**, https://doi.org/10.1175/EI-D-17-0029.1

Parvini, S., B. Poston, A. Jennings, and T. Watanabe, 2019: Storm that pounded Southern California on Saturday will ease up the next few days, forecasters say. *Los Angeles Times*, accessed 21 November 2019, https://www.latimes.com/local/lanow/la-me-ln-southern-california-storms-20190202-story.html.

Persson, P. O., P. J. Neiman, B. Walter, J. Bao, and F. M. Ralph, 2005: Contributions from California coastal-zone surface fluxes to heavy coastal precipitation: A CALJET case study during the strong El Niño of 1998. *Mon. Wea. Rev.*, **133**, 1175–1198, https://doi.org/10.1175/MWR2910.1.

Petterssen, S., 1936: Contribution to the theory of frontogenesis. *Geofys. Publ.*, **11**, 1–27.

Pleim, J. E., 2007: A combined local and nonlocal closure model for the atmospheric boundary layer. Part I: Model description and testing. *J. Appl. Meteor. Climatol.*, **46**, 1383–1395, https://doi.org/10.1175/JAM2539.1.

Prein, A. F., R. M. Rasmussen, K. Ikeda, C. Liu, M. P. Clark, and G. J. Holland, 2017: The future intensification of hourly precipitation extremes. *Nat. Climate Change*, **7**, 48–52, https://doi.org/10.1038/nclimate3168.

Ralph, F. M., and Coauthors, 2020: West Coast forecast challenges and development of atmospheric river reconnaisance. *Bull. Amer. Meteor. Soc.*, **101**, E1357–E1377, https://doi.org/10.1175/BAMS-D-19-0183.1.

Rodwell, M. J., S. T. K. Lang, N. B. Ingleby, N. Bormann, E. Hólm, F. Rabier, D. S. Richardson, and M. Yamaguchi, 2016: Reliability in ensemble data assimilation. *Quart. J. Roy. Meteor. Soc.*, **142**, 443–454, https://doi.org/10.1002/qj.2663.

Saha, S., and Coauthors, 2010: The NCEP Climate Forecast System Reanalysis. *Bull. Amer. Meteor. Soc.*, **91**, 1015–1058, https://doi.org/10.1175/2010BAMS3001.1.

Shapiro, M. A., and D. Keyser, 1990: Fronts, jet streams and the tropopause. *Extratropical Cyclones*, C. W. Newton and E. O. Holopainen, Eds., Amer. Meteor. Soc., 167–191.

Skamarock, W. C., and Coauthors, 2008: A description of the Advanced Research WRF version 3. NCAR Tech. Note NCAR/TN-475+STR, 113 pp., https://doi.org/10.5065/D68S4MVH.

Staley, D. M., J. W. Kean, S. H. Cannon, K. Schmidt, and J. L. Laber, 2013: Objective definition of rainfall intensity–duration thresholds for the initiation of post-fire debris flows in southern California. *Landslides*, **10**, 547–562, https://doi.org/10.1007/s10346-012-0341-9.

Stensrud, D. J., and Coauthors, 2009: Convective-scale warn-on-forecast system. *Bull. Amer. Meteor. Soc.*, **90**, 1487–1500, https://doi.org/10.1175/2009BAMS2795.1.

Sukup, S. J., J. Laber, D. Sweet, and R. Thompson, 2015: Analysis of an intense narrow cold frontal rainband and the Springs Fire burn area debris flow of 12 December 2014. NWS Tech. Attachment 1601, 32 pp., http://www.wrh.noaa.gov/media/wrh/online_publications/TAs/TA1601.pdf.

Thompson, G., P. R. Field, R. M. Rasmussen, and W. D. Hall, 2008: Explicit forecasts of winter precipitation using an improved bulk microphysics scheme. Part II: Implementation of a new snow parameterization. *Mon. Wea. Rev.*, **136**, 5095–5115, https://doi.org/10.1175/2008MWR2387.1.

Times Staff, 2019: Powerful storm brings a traffic nightmare; motorists urged to limit non-essential travel. *Los Angeles Times*. Accessed 21 November 2019, https://www.latimes.com/local/lanow/la-me-rain-freeways-accidents-20190202-story.html.

U.S. Census Bureau, 2019: *Quick Facts*. Accessed 23 September 2019, https://www.census.gov/quickfacts.

U.S. Geological Survey (USGS), 2005: Southern California—Wildfires and debris flows. USGS Fact Sheet 2005–3106, 4 pp., https://pubs.usgs.gov/fs/2005/3106/.

——, 2019: Emergency assessment of post-fire debris-flow hazards. Accessed 3 October 2019, https://landslides.usgs.gov/hazards/postfire_debrisflow/.

Viale, M., R. A. Houze, and K. L. Rasmussen, 2013: Upstream orographic enhancement of a narrow cold-frontal rainband approaching the Andes. *Mon. Wea. Rev.*, **141**, 1708–1730, https://doi.org/10.1175/MWR-D-12-00138.1.

Wakimoto, R. M., and B. L. Bosart, 2000: Airborne radar observations of a cold front during FASTEX. *Mon. Wea. Rev.*, **128**, 2447–2470, https://doi.org/10.1175/1520-0493(2000)128<2447:AROOAC>2.0.CO;2.

Warner, T. T., 2011: *Numerical Weather and Climate Prediction*. Cambridge University Press, 526 pp.

Westra, S., and Coauthors, 2014: Future changes to the intensity and frequency of short-duration extreme rainfall. *Rev. Geophys.*, **52**, 522–555, https://doi.org/10.1002/2014RG000464.

Wills, C. J., N. E. Roth, T. P. McCrink, and W. R. Short, 2017: The California landslide inventory database. *Proc. Third North American Symp. on Landslides*, Roanoke, VA, Association of Environmental and Engineering Geologists, 666–674.